INTERNATIONAL JOURNAL FOR NUMERICAL METHODS IN FLUIDS, VOL. 12, 261–285 (1991)

A COMPUTATIONAL METHOD FOR THE HYDRODYNAMICS OF FRACTURED–POROUS MEDIA

G. M. GRANDI AND J. C. FERRERI*

CNEA, Gerencia Prot. Rad. y Seguridad, Av. Libertador 8250, 1429 Buenos Aires, Argentina

SUMMARY

A numerical method based on the boundary-fitted finite difference method (BFDM) is presented in this paper. The boundaries are external (the boundary of the physical domain) and internal (which corresponds to the fracture network). The difference between this approach and the usual one lies in the inclusion of discrete fractures in the volume that represents the porous medium. The numerical model has been used in the prediction of the flow pattern in several internationally recognized verification cases and applied to the solution of hypothetical problems of interest to us in the field of nuclear waste repository modelling. The results obtained show that the numerical approach considered gives accurate and reliable predictions of the hydrodynamics of fractured–porous media, thus justifying its use for the above-mentioned studies.

KEY WORDS Boundary-fitted finite difference method Fractured–porous media Ground water flow High level radioactive wastes Radionuclide migration Repositories modelling

INTRODUCTION

The prediction of the flow pattern of buoyancy- and pressure-driven flows in fractured–porous media has important technological applications. Geothermal and petroleum reservoir engineering, the prediction of the impact of nuclear waste repository emplacements and many other applications justify the ever-growing interest in this subject.

This paper resulted from the authors' interest in the field of nuclear waste repository emplacements.[1–4] The accurate prediction of the hydrodynamics of such repositories is of primary importance for the assessment of the radiological safety and subsequent licensing of those facilities. The present paper is a full description of the algorithms used to solve the problems of fluid flow, heat transfer and radionuclide migration in a fractured–porous medium.

The conceptual model of the flow and heat transfer in a porous–fractured medium is considered now. A typical structure of a granitic mass, suitable for use as a potential site for repository emplacement, may be viewed as large blocks of quasi-homogeneous rock surrounded and/or intersected by fractured zones. The influence of microfractures (included in the otherwise homogeneous rock) and macrofractures (or discrete fractures), mainly responsible for the flow pattern configuration, may be described by different approximations.

Continuum approximation

The equivalent porous medium and the double-porosity method are examples of this approach. In the equivalent porous medium approximation the rock mass including the fractured zones is

* Member of Carrera del Investigador, CONICET, Argentina.

0271–2091/91/030261–25$12.50
© 1991 by John Wiley & Sons, Ltd.
Received 16 June 1989
Revised 20 February 1990

described on a large scale, so that properties (porosity, permeability) and parameters (temperature, pressure, velocity) are averaged in large blocks. In this way an idealized equivalent porous medium replaces the actual one. The equivalent medium is non-isotropic and the average properties depend not only on the fluid and rock properties but also on the boundary conditions. In Reference 5 a technique was developed to obtain average properties for the representation of fractured–porous media. The equivalent porous medium gives good results only for a global-scale model without much detail. In the double-porosity approximation the flow region is idealized as two interacting media: one representing the fracture system and the other representing the porous medium. This system can be described by two sets of conservation equations, one for each medium. The equations are linked by non-linear source terms depending on the potential in each medium. This model allows easy analytical treatment of anisotropic problems and the bulk properties do not depend on the boundary conditions. On the other hand, as Narasimhan[6] pointed out, the multivalued fluid flow field may not be the best input to solve the radionuclide transport equation.

Discrete approximation

The rock matrix is idealized as large blocks of impermeable material surrounded by a network of discrete fractures where the fluid flows. It is similar to a net of conduits and does not take into account the fluid flow in the porous medium. See Reference 7 and the references cited therein as an example of this approach.

Equivalent porous medium and discrete fracture approximation

This model combines the continuous approximation for the porous rock matrix and the discrete approximation for the fracture network. The properties in the bulk media are obtained by averages. This task is now easily performed because the anisotropies of the actual media are taken into account by the fracture network. The integral formulation of the mass conservation equation avoids the source terms and the internal boundary conditions between the fractures and the porous medium. The integral finite difference method of Narasimhan[6, 8] and the finite element method developed by Baca *et al.*[9] belong to this approach. This approximation is used as the conceptual model in the present work.

In the following section the governing equations in the physical domain are introduced. Later on, the basis of the BFDM is presented in order to derive the governing equations in the computational domain. The discretization of the resulting equations is also shown, along with some computational details. Finally, several examples of verification and particular applications are shown.

GOVERNING EQUATIONS

The equations that govern the flow in a rock traversed by discrete fractures are considered in this section. The validity of Darcy's and Boussinessq's approximations to the Navier–Stokes equations is accepted for the flow, both in the equivalent porous medium and in the discrete fractures. The equations are:

(i) the momentum equations in the porous medium,

$$\mathbf{u} = -\frac{k_p}{\nu}(\nabla P + \mathbf{g}\beta\Delta T); \tag{1}$$

(ii) the momentum equations in the fractures,

$$\mathbf{u}_f = -\frac{k_f}{\nu}[(\nabla P \cdot \boldsymbol{\iota})\boldsymbol{\iota} + \beta(\mathbf{g}\cdot\boldsymbol{\iota})\boldsymbol{\iota}\Delta T]; \tag{2}$$

(iii) the mass conservation equation in a volume of porous–fractured rock,

$$\int_{V_p} S^p \frac{\partial p}{\partial t}\,dV + \int_{V_f} S^f \frac{\partial p}{\partial t}\,dV + \int_V \nabla\cdot(\rho\mathbf{u})\,dV + \int_{\partial V_{f,ext}} \rho(\mathbf{u}_f\cdot\mathbf{n})\,dA = 0; \tag{3}$$

(iv) the energy conservation equation in a volume of porous–fractured rock:

$$(\rho c)^p \frac{\partial T}{\partial t} + (\rho c)^{fl}\mathbf{u}\cdot\nabla T = \nabla\cdot(\Gamma^p\nabla T) + Q; \tag{4}$$

(v) the radionuclide transport equation in a volume of porous–fractured rock:

$$\int_{V-V_f} R_p\phi\left(\frac{\partial C}{\partial t} + \lambda C\right)dV + \int_{V_f} R_f\left(\frac{\partial C}{\partial t} + \lambda C\right)dV + \int_V \mathbf{u}\cdot\nabla C\,dV - \int_V \nabla\cdot(D_p\nabla C)\,dV + \int_{\partial V_{f,ext}} (\mathbf{u}_f\cdot\mathbf{n})C - \left(D_f\frac{\partial C}{\partial \boldsymbol{\iota}}\cdot\mathbf{n}\right)dV = 0. \tag{5}$$

In equations (1)–(5) the meaning of the variables is as follows:

c	specific heat capacity
C	radionuclide concentration
k	permeability
D	diffusion coefficient
$\mathbf{g}$	acceleration due to gravity
P	(pressure − hydrostatic head)/ρ_0
Q	thermal heat source
R	retention factor for a radionuclide
S	specific storage
T	temperature
$\mathbf{u}$	volume-averaged fluid velocity
$\mathbf{u}_f$	fluid velocity in the discrete fractures
β	fluid thermal expansion coefficient
ϕ	porosity
Γ	thermal conductivity
λ	radionuclide decay constant
ν	kinematic viscosity
ρ	density
∇	nabla operator
$\boldsymbol{\iota}$	unit vector in the direction of a fracture
$\mathbf{n}$	unit vector normal to a volume surface
∂V	volume boundary
V	control volume,

The subscripts and superscripts represent:

p	porous medium
f	fracture
fl	fluid
0	reference value for Boussinesseq's expansion
ext	fracture surface on the faces of the control volume.

In equations (1)–(5) it is assumed that the fluid properties are not temperature-dependent. The extension to consider variable properties is straightforward.

The determination of k_p for the porous matrix is simple because it is considered as data. The corresponding value for the fractures is obtained by assuming that the flow satisfies the Poiseuille flow law (cubic law for flow rates). This in turn implies that

$$k_f = b^2/12,$$

where b is the aperture of the fracture. In the codes the fracture permeability is usually made to follow this law. In some other cases the fractures are considered to be filled with a porous material of a given permeability (linear law for flow rates).

The surface integrals in equations (3)–(5) must be interpreted as measuring the contribution of the flow along the fractures to the balance of a parameter. The surface ∂V_{ext} is the fraction of the total volume surface corresponding to the fracture cross-sectional area and does not include the fracture within the control volume. Equation (3) is valid for a saturated, fractured–porous, consolidating medium. However, in most cases the rock can be considered as non-deformable and the fluid as incompressible. This is easily done by setting S^f and S^p equal to zero. Equation (4) implies thermal equilibrium between the rock and the fluid and neglect of the advective terms. These facts are a limitation of the present analysis. However, if the Rayleigh number is not very high, they do not have any practical consequence, even for the fractures.[10] Equation (5) implies (a) saturation of the porous medium and the fractures, (b) that the solute is inert (this means that it does not affect the physical properties of the fluid) and (c) that the rock matrix is non-deformable.

NUMERICAL METHOD

The numerical solution of equations (1)–(5) is found by means of the BFDM. A detailed description of the method can be found, for example, in Reference 11. The transformed equations for two-dimensional isothermal flow are given in Reference 3. Since the present approach is somewhat different from the usual ones in the BFDM, some algebraic details will be shown in this section, but for the sake of brevity only in two space dimensions. The extension to three dimensions is straightforward.

The arbitrary physical domain $\mathbb{L}(x, y)$ is transformed into a regular one denoted by $\mathbb{L}'(U, V)$ (this will be called the computational domain from now on) in order to solve the governing equations (1)–(5) by means of the BFDM. The co-ordinates in the computational plane are

$$U = U(x, y), \qquad V = V(x, y). \tag{6}$$

If the Jacobian of the transformation does not vanish the transformation can be inverted:

$$x = X(U, V), \qquad y = Y(U, V). \tag{7}$$

Figure 1 shows a cell belonging to a hypothetical grid and illustrates the location of the variables. As can be seen, velocities are located at the cell corners. Pressure, temperature and

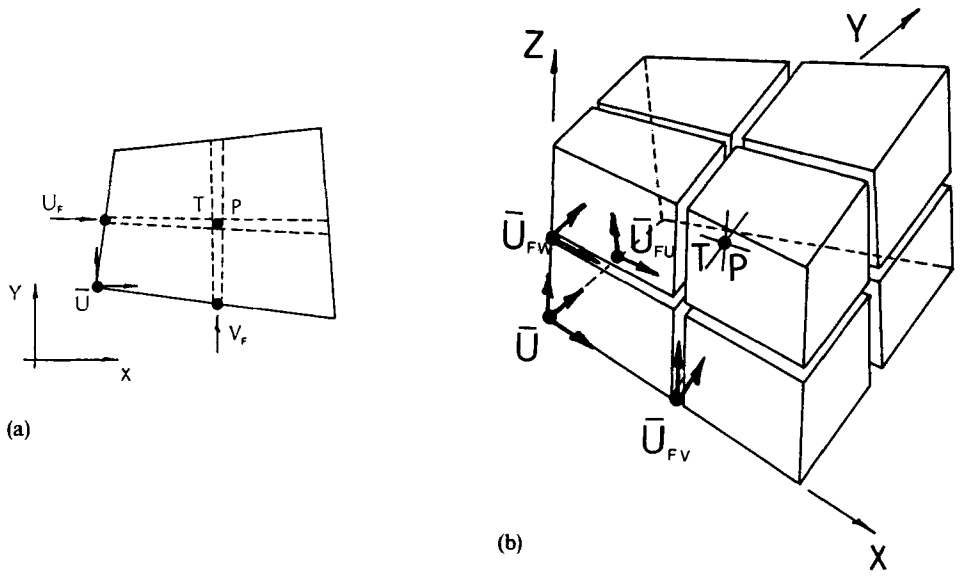

Figure 1. Location of the variables in a computational cell: (a) 2D cell; (b) 3D cell

scalar concentration are located at the cell centroid. $D_{i,j}$, the discrete analogue of the flow divergence, is also located at the cell centroid.

Two paths crossing at the centroid of the cell, representing one-dimensional links between pressure nodes, are also shown in Figure 1(a). These paths are the discrete images of the fractures in the rock. Thus the representation of the structure of the rock consists of large blocks of an equivalent, homogeneous, porous continuum surrounded by discrete one-dimensional fractures. The velocities along the fractures are called u_f and v_f respectively.

It is interesting to point out that this particular centring of the variables forces the fractures to be coincident with lines joining the centroids of the cells. Then the BFDM is used to fit 'internal' boundaries as well as external ones. Consequently, u_f and v_f can be considered as the moduli of vectors tangent to the lines of constant values of the co-ordinate in the computational plane. The inclusion of the discrete fracture representation in the volume that represents the porous medium constitutes, to the authors' knowledge, the difference between the usual approach and the present one.

The integration domain is subdivided into a number of discrete cells such as that shown in Figure 1. The 1D paths representing the fractures are set logically to 'on' in order to include fractures crossing control volumes. In this way only those cells including fractures take into account the effects of the 1D paths. Otherwise they work as homogeneous volumes of porous media with the corresponding fracture parameters set to zero.

In the 3D case the fractures are planes of varying aperture and two velocity components have been allowed for them, centred at the midpoints of the edges of the control volume. In addition, tubes connecting opposite face centroids are also considered. This in turn allows for a simple reduction from 3D to 2D flow descriptions. Figure 1(b) shows this set of variables in a 3D representation.

Hydrodynamic problem (mass and momentum equations)

Considering the co-ordinate transformation (7), the momentum and mass conservation equations (1)–(3) can be written as

$$u=-\frac{k_p}{\nu}\left(\mathrm{AUX}\frac{\partial P}{\partial U}+\mathrm{AVX}\frac{\partial P}{\partial V}\right), \tag{8a}$$

$$v=-\frac{k_p}{\nu}\left(\mathrm{AUY}\frac{\partial P}{\partial U}+\mathrm{AVY}\frac{\partial P}{\partial V}+\beta g\,\Delta T\right), \tag{8b}$$

$$u_f=-\frac{k_f}{\nu}\left(\mathrm{EUU}\frac{\partial P}{\partial U}+\beta g_U\Delta T\right), \tag{9a}$$

$$v_f=-\frac{k_f}{\nu}\left(\mathrm{FVV}\frac{\partial P}{\partial V}+\beta g_v\Delta T\right), \tag{9b}$$

$$\left\langle S^p\frac{\partial P}{\partial t}\right\rangle(V-V_f)+\left\langle S^f\frac{\partial P}{\partial t}\right\rangle V_f+V\left[x^{-m}\left(\mathrm{BUX}\frac{\partial\rho u x^m}{\partial U}+\mathrm{BVX}\frac{\partial\rho u x^m}{\partial V}\right)\right.$$
$$\left.+\left(\mathrm{BUY}\frac{\partial\rho v}{\partial U}+\mathrm{BVY}\frac{\partial\rho v}{\partial V}\right)\right]+\rho u_{fe}b_e\cos\alpha_e+\rho v_{fn}b_n\cos\alpha_n-\rho u_{fw}b_w\cos\alpha_w-\rho v_{fs}b_s\cos\alpha_s=0, \tag{10}$$

where $m=1$ for cylindrical co-ordinates and $m=0$ for Cartesian co-ordinates.

The various coefficients in equations (8)–(10) measure the influence of the co-ordinate transformation upon the original equations. The coefficients AUX, etc. are calculated as corner-centred coefficients:

$$\begin{aligned}
&\mathrm{AUX}=U_x=Y_v/J, && \mathrm{AUU}=U_x^2+U_y^2,\\
&\mathrm{AUY}=U_y=-X_v/J, && \mathrm{AUV}=U_xV_x+V_yU_y,\\
&\mathrm{AVX}=V_x=-Y_u/J, && \mathrm{AVU}=\mathrm{AUV},\\
&\mathrm{AVY}=V_y=X_u/J, && \mathrm{AVV}=V_x^2+V_y^2,
\end{aligned}$$

where J is the Jacobian of the transformation, given by

$$J=X_uY_v-X_vY_u.$$

The coefficients EUU, EVV, g_u and g_v are calculated at the centre of the cell faces:

$$\mathrm{EUU}=(U_xV_y-V_xU_y)/\sqrt{(\mathrm{AVV})},$$
$$\mathrm{FVV}=(U_xV_y-V_xU_y)/\sqrt{(\mathrm{AUU})},$$
$$g_u=-gV_x/\sqrt{(\mathrm{AVV})},\qquad g_v=-gU_x/\sqrt{(\mathrm{AUU})},$$
$$\cos\alpha=(U_xV_y-V_xU_y)/\sqrt{(\mathrm{AUU})}\sqrt{(\mathrm{AVV})},$$

where AUU and AVV are now appropriately averaged in the faces. The coefficients denoted by BUX, etc. have the same meaning as AUX, etc. and only differ in their location at the grid, representing the cell-centred transformation coefficients.

The discrete versions of equations (8)–(10) are obtained by means of centred difference approximations in the computational plane, implying an appropriate averaging of the variables

in the cell. The discrete approximations are written as:

(i) u-momentum equation (8a),

$$\mathbb{A}_0 u_{i,j} = \mathbb{A}_1 p_{i,j} + \mathbb{A}_2 p_{i-1,j} + \mathbb{A}_3 p_{i,j-1} + \mathbb{A}_4 p_{i-1,j-1}, \tag{11}$$

where

$$\begin{aligned}
&\mathbb{A}_0 = 1,\\
&\mathbb{A}_1 = (k_p/2\mu)(-\mathrm{AUX}_{i,j} - \mathrm{AVX}_{i,j}),\\
&\mathbb{A}_2 = (k_p/2\mu)(+\mathrm{AUX}_{i,j} - \mathrm{AVX}_{i,j}),\\
&\mathbb{A}_3 = (k_p/2\mu)(-\mathrm{AUX}_{i,j} + \mathrm{AVX}_{i,j}),\\
&\mathbb{A}_4 = (k_p/2\mu)(+\mathrm{AUX}_{i,j} + \mathrm{AVX}_{i,j});
\end{aligned}$$

(ii) v-momentum equation (8b),

$$\mathbb{B}_0 u_{i,j} = \mathbb{B}_1 p_{i,j} + \mathbb{B}_2 p_{i-1,j} + \mathbb{B}_3 p_{i,j-1} + \mathbb{B}_4 p_{i-1,j-1} + \mathbb{B}_5, \tag{12}$$

where

$$\begin{aligned}
&\mathbb{B}_0 = 1,\\
&\mathbb{B}_1 = (k_p/2\mu)(-\mathrm{AUY}_{i,j} - \mathrm{AVY}_{i,j}),\\
&\mathbb{B}_2 = (k_p/2\mu)(+\mathrm{AUY}_{i,j} - \mathrm{AVY}_{i,j}),\\
&\mathbb{B}_3 = (k_p/2\mu)(-\mathrm{AUY}_{i,j} + \mathrm{AVY}_{i,j}),\\
&\mathbb{B}_4 = (k_p/2\mu)(+\mathrm{AUY}_{i,j} + \mathrm{AVY}_{i,j}),\\
&\mathbb{B}_5 = -\beta g \Delta T_{i,j};
\end{aligned}$$

(iii) u_f-momentum equation (9a),

$$\mathbb{C}_0 u_{fi,j} = \mathbb{C}_1 p_{i-1,j} + \mathbb{C}_2 p_{i,j} + \mathbb{C}_3, \tag{13}$$

where

$$\begin{aligned}
&\mathbb{C}_0 = 1,\\
&\mathbb{C}_1 = (k_f/\mu)\,\mathrm{EUU}_{i,j},\\
&\mathbb{C}_2 = (k_f/\mu)(-\mathrm{EUU}_{i,j}),\\
&\mathbb{C}_3 = -\beta g_u \Delta T_{i+1/2,j};
\end{aligned}$$

(iv) v_f-momentum equation (9b),

$$\mathbb{D}_0 u_{fi,j} = \mathbb{D}_1 p_{i,j-1} + \mathbb{D}_2 p_{i,j} + \mathbb{D}_3, \tag{14}$$

where

$$\begin{aligned}
&\mathbb{D}_0 = 1,\\
&\mathbb{D}_1 = (k_f/\mu)\,\mathrm{FVV}_{i,j},\\
&\mathbb{D}_2 = (k_f/\mu)(-\mathrm{FVV}_{i,j}),\\
&\mathbb{D}_3 = -\beta g_v \Delta T_{i,j+1/2};
\end{aligned}$$

(v) mass conservation equation (10),

$$\mathbb{E}_0 p_{i,j} - \mathbb{E}_1 p^n_{i,j} = D_{i,j}, \tag{15a}$$

where

$$\begin{aligned}
D_{i,j} = {} & \mathbb{E}_2 u_{i+1,j+1} + \mathbb{E}_3 u_{i+1,j} + \mathbb{E}_4 u_{i,j+1} + \mathbb{E}_5 u_{i,j} + \mathbb{E}_6 v_{i+1,j+1} + \mathbb{E}_7 v_{i+1,j}\\
& + \mathbb{E}_8 v_{i,j+1} + \mathbb{E}_9 v_{i,j} + \mathbb{E}_{10} u_{fi,j} + \mathbb{E}_{11} u_{fi+1,j} + \mathbb{E}_{12} v_{i,j} + \mathbb{E}_{13} v_{fi,j+1},
\end{aligned} \tag{15b}$$

with

$$\mathbb{E}_0=(S_p/\delta t)(\mathscr{V}-V_f)+(S_f/\delta t)V_f,$$
$$\mathbb{E}_1=\mathbb{E}_0,$$
$$\mathbb{E}_2=(\mathscr{V}/2)x^m_{i+1,j+1}(-\mathrm{BUX}_{i,j}-\mathrm{BVX}_{i,j})\bar{x}^m_{i+1/2,j+1/2},$$
$$\mathbb{E}_3=(\mathscr{V}/2)x^m_{i+1,j}(-\mathrm{BUX}_{i,j}+\mathrm{BVX}_{i,j})\bar{x}^m_{i+1/2,j+1/2},$$
$$\mathbb{E}_4=(\mathscr{V}/2)x^m_{i,j+1}(\mathrm{BUX}_{i,j}-\mathrm{BVX}_{i,j})\bar{x}^m_{i+1/2,j+1/2},$$
$$\mathbb{E}_5=(\mathscr{V}/2)x^m_{i+1,j+1}(\mathrm{BUX}_{i,j}+\mathrm{BVX}_{i,j})\bar{x}^m_{i+1/2,j+1/2},$$
$$\mathbb{E}_6=(\mathscr{V}/2)(-\mathrm{BUX}_{i,j}-\mathrm{BVX}_{i,j}),$$
$$\mathbb{E}_7=(\mathscr{V}/2)(-\mathrm{BUX}_{i,j}+\mathrm{BVX}_{i,j}),$$
$$\mathbb{E}_8=(\mathscr{V}/2)(\mathrm{BUX}_{i,j}-\mathrm{BVX}_{i,j}),$$
$$\mathbb{E}_9=(\mathscr{V}/2)(\mathrm{BUX}_{i,j}+\mathrm{BVX}_{i,j}),$$
$$\mathbb{E}_{10}=+b_w\cos\alpha_w,\qquad \mathbb{E}_{12}=+b_s\cos\alpha_s,$$
$$\mathbb{E}_{11}=-b_e\cos\alpha_e,\qquad \mathbb{E}_{13}=-b_n\cos\alpha_n.$$

The different algorithms used to solve the difference equations (11)–(15) are discussed below.

First, the incompressible flow in a consolidated medium, i.e. incompressible flow in a non-deformable rock matrix, is considered. This implies that S^p and S^f are set equal to zero. The flow is solved in terms of primitive variables (P, u, v, u_f, v_f) or in terms of the pressure (P) only. In both cases, iterative or direct solvers are used.

The iterative algorithm, in primitive variables, is of the semi-implicit type. First, the energy equation (see next section) is advanced from time $n\delta t$ to time $(n+1)\,\delta t$ to produce the driving force in the momentum equations. The calculation follows with a guessed pressure field (taken as P^n), giving approximate values for the velocities from the momentum equations (11)–(14). Then the following iterative method is applied.

(i) The discrete analogue of the cell divergence $D_{i,j}$ is obtained (via equation (15a)).

(ii) The pressure in the cell is adjusted to bring the cell divergence to zero as follows:

$$P_{i,j}=P_{i,j}+\delta P_{i,j},$$

where

$$\delta P_{i,j}=-\frac{\omega D_{i,j}}{\partial D_{i,j}/\partial P_{i,j}},$$

with

$$\frac{\partial D}{\partial P}=\frac{1}{k_p/v}\Bigg(\mathrm{BUX}_{i,j}\frac{V}{4}\bar{x}^m_{i+1/2,j+1/2}(\mathrm{AUX}_{i+1,j+1}x^m_{i+1,j+1}+\mathrm{AUX}_{i+1,j}x^m_{i+1,j}$$
$$+\mathrm{AUX}_{i,j+1}x^m_{i,j+1}+\mathrm{AUX}_{i,j}x^m_{i,j})+\mathrm{BVX}_{i,j}\frac{V}{4}\bar{x}^m_{i+1/2,j+1/2}(\mathrm{AUX}_{i+1,j+1}x^m_{i+1,j+1}$$
$$+\mathrm{AVX}_{i+1,j}x^m_{i+1,j}+\mathrm{AVX}_{i,j+1}x^m_{i,j+1}+\mathrm{AVX}_{i,j}x^m_{i,j})+\mathrm{BUY}_{i,j}\frac{V}{4}(\mathrm{AUY}_{i+1,j+1}$$
$$+\mathrm{AUY}_{i+1,j}+\mathrm{AUX}_{i,j+1}+\mathrm{AUX}_{i,j})+\mathrm{BVY}_{i,j}\frac{V}{4}(\mathrm{AVY}_{i+1,j+1}$$

$$+\mathrm{AVY}_{i+1,j}+\mathrm{AVX}_{i,j+1}+\mathrm{AVX}_{i,j})\Big)^{-1}+\frac{1}{k_f/v}(\mathrm{EUU}_{i,j}b_w\cos\alpha_w$$
$$+\mathrm{EUU}_{i+1,j}b_e\cos\alpha_e+\mathrm{FVV}_{i,j}b_s\cos\alpha_s+\mathrm{FVV}_{i,j+1}b_n\cos\alpha_n)^{-1}.$$

Here ω is an overrelaxation factor, set to 1·7 for this type of problems.

(iii) The velocity components are modified accordingly with the new pressure field as follows:

$$u_{i+1,j+1}^{(k+1)}=u_{i+1,j+1}^{(k)}+C(\mathrm{AUX}_{i+1,j+1}+\mathrm{AVX}_{i+1,j+1}),$$
$$u_{i+1,j}^{(k+1)}=u_{i+1,j}^{(k)}+C(\mathrm{AUX}_{i+1,j}-\mathrm{AVX}_{i+1,j}),$$
$$u_{i,j+1}^{(k+1)}=u_{i,j+1}^{(k)}+C(-\mathrm{AUX}_{i,j+1}+\mathrm{AVX}_{i,j+1}),$$
$$u_{i,j}^{(k+1)}=u_{i,j}^{(k)}+C(-\mathrm{AUX}_{i,j}-\mathrm{AVX}_{i,j}),$$
$$v_{i+1,j+1}^{(k+1)}=v_{i+1,j+1}^{(k)}+C(\mathrm{AUY}_{i+1,j+1}+\mathrm{AVY}_{i+1,j+1}),$$
$$v_{i+1,j}^{(k+1)}=v_{i+1,j}^{(k)}+C(\mathrm{AUY}_{i+1,j}-\mathrm{AVY}_{i+1,j}),$$
$$v_{i,j+1}^{(k+1)}=v_{i,j+1}^{(k)}+C(-\mathrm{AUY}_{i,j+1}+\mathrm{AVY}_{i,j+1}),$$
$$v_{i,j}^{(k+1)}=v_{i,j}^{(k)}+C(-\mathrm{AUY}_{i,j}-\mathrm{AVY}_{i,j}),$$
$$u_{fi+1,j}^{(k+1)}=u_{fi+1,j}^{(k)}+C_f\,\mathrm{EUU}_{i+1,j},$$
$$u_{fi,j}^{(k+1)}=u_{fi,j}^{(k)}-C_f\,\mathrm{EUU}_{i,j},$$
$$v_{fi,j+1}^{(k+1)}=v_{fi,j+1}^{(k)}+C_f\,\mathrm{FVV}_{i,j+1},$$
$$v_{fi,j}^{(k+1)}=v_{fi,j}^{(k)}-C_f\,\mathrm{FVV}_{i,j},$$

where C and C_f are defined as

$$C=(k_p/2)\delta P_{i,j},\qquad C_f=k_f\delta P_{i,j}.$$

(iv) Boundary conditions are appropriately applied after each iteration sweep. Steps (i)–(iv) are repeated until a suitable norm for $D_{i,j}$ is below a given tolerance.

Such as presented, the iterative algorithm solves the Poisson equation for the pressure through the use of an intermediate variable (D) and provides a simultaneous adjustment of velocities. An alternative approach consists of solving the Poisson equation for the pressure directly. Its discrete version is

$$\mathbb{F}_0P_{i,j}+\mathbb{F}_1P_{i-1,j}+\mathbb{F}_2P_{i+1,j}+\mathbb{F}_3P_{i,j-1}+\mathbb{F}_4P_{i,j+1}+\mathbb{F}_5P_{i-1,j-1}+\mathbb{F}_5P_{i+1,j+1}$$
$$+\mathbb{F}_6P_{i-1,j+1}+\mathbb{F}_6P_{i+1,j-1}=\mathbb{F}_0P_{i,j}^n, \tag{16}$$

where

$$\mathbb{F}_0=k_pV(2\,\mathrm{AUU}_{i,j}+2\,\mathrm{AVV}_{i,j})+k_f(\mathrm{EUU}_{i,j}b_w\cos\alpha_w+\mathrm{EUU}_{i+1,j}b_e\cos\alpha_e$$
$$+\mathrm{FVV}_{i,j}b_s\cos\alpha_s+\mathrm{FVV}_{i,j+1}b_n\cos\alpha_n),$$
$$\mathbb{F}_1=k_pV[-\mathrm{AUU}_{i,j}+(\mathrm{AU}_{i,j}+mx^{-m}\mathrm{AUX}_{i,j})/2-k_f\mathrm{EUU}_{i,j}b_w\cos\alpha_w],$$
$$\mathbb{F}_2=k_pV[-\mathrm{AUU}_{i,j}+(-\mathrm{AU}_{i,j}-mx^{-m}\mathrm{AUX}_{i,j})/2-k_f\mathrm{EUU}_{i+1,j}b_e\cos\alpha_e],$$
$$\mathbb{F}_3=k_pV[-\mathrm{AVV}_{i,j}+(\mathrm{AV}_{i,j})/2-k_f\mathrm{FVV}_{i,j}b_s\cos\alpha_s],$$
$$\mathbb{F}_4=k_pV[-\mathrm{AVV}_{i,j}+(-\mathrm{AV}_{i,j})/2-k_f\mathrm{FVV}_{i,j+1}b_n\cos\alpha_n],$$
$$\mathbb{F}_5=-k_pV\,\mathrm{AVV}_{i,j}/4,$$
$$\mathbb{F}_6=-\mathbb{F}_5.$$

This procedure was also implemented and the error of the computed solution is sometimes less sensitive to steep variations in pressure.

The other algorithm implies the use of a direct solver in order to obtain a fully coupled solution of equations (11)–(15). The equations are ordered by block, each one representing a computational cell. In each block the equations are ordered as follows:

(i) u-momentum (from which u is obtained)
(ii) continuity (from which v is obtained)
(iii) v-momentum (from which P is obtained)
(iv) u_f-momentum (from which u_f is obtained)
(v) v_f-momentum (from which v_f is obtained).

Boundary conditions are incorporated explicitly in the system of equations.

The algebraic system of linear equations is solved with a library sparse matrix solver named MA28AD from the Harwell package,[12] which proved to be efficient in most cases. However, attention must be paid to the relative weight of the coefficients in order to obtain meaningful results.

Different boundary conditions may be prescribed, namely:

(i) inflow–outflow boundaries, with both rock and fracture fluid velocities specified
(ii) free-slip boundaries, where the normal component of the velocity vector is null—in this case the velocity at the boundary is obtained from the velocity at an inner point as in Reference 11, i.e.

$$\mathbf{u}_B = (\mathbf{u}_I \cdot \mathbf{n})\mathbf{n} - \mathbf{u}_I,$$

where I and B represent the inner and boundary points respectively and $\mathbf{n}$ is the unit vector normal to the boundary
(iii) boundaries with imposed pressure
(iv) periodic boundaries, where the inflow and outflow are linked by periodicity.

In the direct method the imposition of the boundary conditions also implies the reordering of equations in the cells adjacent to the physical boundaries (see Reference 13 for a complete description). For example, if the pressure is specified at a boundary, the equations are ordered as follows:

(i) u-momentum (from which u is obtained)
(ii) v-momentum (from which v is obtained)
(iii) boundary condition (from which P is obtained)
(iv) u_f-momentum (from which u_f^f is obtained)
(v) v_f-momentum (from which v_f is obtained).

This is not the case with the iterative procedure.

Both algorithms should be modified [14,15] in problems with large pressure gradients if a relatively coarse grid is used. The iterative algorithm is modified as follows.

(i) The velocities in the rock and in the fractures are calculated via equations (11)–(14).
(ii) The discrete analogue of the divergence $D_{i,j}$ is calculated via equation (15a).
(iii) $D_{i,j}$ is redefined as

$$D_{i,j} = D_{i,j} + D_{\mathrm{h}\,i,j},$$

where $D_{\mathrm{h}\,i,j}$ is the divergence of the velocity field obtained from the velocities calculated with the *discrete analogue* of (11)–(14) and a local semi-analytic distribution of pressure.
(iv) Follow with the standard iteration.

As may be seen from the above description, the only difference consists of considering the known behaviour of the solution in the vicinity of the zones with steep gradients. It must be mentioned that this procedure of singularity extraction in a semi-implicit code is the only way the authors know to get a correct solution under such an approximation.

In the case of a consolidating medium (compressible flow and/or deformable rock matrix), equations (11)–(14) are substituted into equation (15). Then the resulting parabolic equation for the pressure is solved. The equation obtained is similar to equation (16), except that $\mathbb{F}_0$ is modified as follows:

$$\mathbb{F}_0 = (S_p/\delta t)(V - V_f) + (S_f/\delta t) V_f + k_p V(2\,\mathrm{AUU}_{i,j} + 2\,\mathrm{AVV}_{i,j}) + k_f(\mathrm{EUU}_{i,j} b_w \cos\alpha_w + \mathrm{EUU}_{i+1,j} b_e \cos\alpha_e + \mathrm{FVV}_{i,j} b_s \cos\alpha_s + \mathrm{FVV}_{i,j+1} b_n \cos\alpha_n).$$

An implicit scheme (see below) is used because of the severe time restrictions imposed by the fracture parameters. A direct algorithm is implemented using the routine MA28AD.[12] The boundary conditions are explicitly incorporated into the system of equations.

Thermal problem (energy equation)

The energy conservation equation (4) is written using the co-ordinate transformation (7) in terms of the computational coordinate U and V as

$$(\rho c)^p \frac{\partial T}{\partial t} + (\rho c)^{f1}\left[u\left(\mathrm{AUX}\frac{\partial T}{\partial U} + \mathrm{AVX}\frac{\partial T}{\partial V}\right) + v\left(\mathrm{AUY}\frac{\partial T}{\partial U} + \mathrm{AVY}\frac{\partial T}{\partial V}\right)\right] = \Gamma^p\left(\mathrm{AUU}\frac{\partial^2 T}{\partial U^2} + \mathrm{AVV}\frac{\partial^2 T}{\partial V^2} + \mathrm{AUV}\frac{\partial^2 T}{\partial U\,\partial V} + (\mathrm{AU} + m\,\mathrm{AUX}\,x^{-m})\frac{\partial T}{\partial u} + (\mathrm{AV} + m\,\mathrm{AVX}\,x^{-m})\frac{\partial T}{\partial V}\right) + Q, \tag{17}$$

where

$$\mathrm{AU} = U_{xx} + U_{yy}, \qquad \mathrm{AV} = V_{xx} + V_{yy}.$$

The discrete version of equation (17) is obtained by means of centred differences in space:

$$\mathbb{G}_0 T_{i,j}^{n+1} + \mathbb{G}_1 T_{i-1,j} + \mathbb{G}_2 T_{i+1,j} + \mathbb{G}_3 T_{i,j-1} + \mathbb{G}_4 T_{i,j+1} + \mathbb{G}_5 T_{i-1,j-1} + \mathbb{G}_5 T_{i+1,j+1} + \mathbb{G}_6 T_{i-1,j+1} + \mathbb{G}_6 T_{i+1,j-1} = \mathbb{G}_7 T_{i,j}^n + \mathbb{G}_8, \tag{18}$$

where

$$\mathbb{G}_0 = (\rho c)^p/\delta t + \Gamma^p(2\,\mathrm{AUU}_{i,j} + 2\,\mathrm{AVV}_{i,j}),$$

$$\mathbb{G}_1 = \Gamma^p[-\mathrm{AUU}_{i,j} + (\mathrm{AU}_{i,j} + mx^{-m}\mathrm{AUX}_{i,j})/2],$$

$$\mathbb{G}_2 = \Gamma^p[-\mathrm{AUU}_{i,j} + (-\mathrm{AU}_{i,j} - mx^{-m}\mathrm{AUX}_{i,j})/2],$$

$$\mathbb{G}_3 = \Gamma^p[-\mathrm{AVV}_{i,j} + (\mathrm{AV}_{i,j})/2],$$

$$\mathbb{G}_4 = \Gamma^p[-\mathrm{AVV}_{i,j} + (-\mathrm{AV}_{i,j})/2],$$

$$\mathbb{G}_5 = -\Gamma^p\mathrm{AUV}_{i,j}/4,$$

$$\mathbb{G}_6 = -\mathbb{G}_5,$$

$$\mathbb{G}_7 = (\rho c)^p/\delta t,$$

$$\mathbb{G}_8 = Q.$$

As it stands, equation (18) may be solved by means of explicit or implicit methods. Numerically, the explicit option consists of considering all the terms on the LHS of the equation evaluated at $t=n\Delta t$. Correspondingly, the implicit option (really a fully implicit one) consists of evaluating all the terms on the LHS of the equation at $t=(n+1)\Delta t$.

The presence of concentrated heat sources introduces some difficulties for the numerical solution of (18). In practice, the approach described in Reference 1 was adopted. These sources can be adequately treated with coarse grids if the solution to the problem

$$\mathbb{L}\{T\}=Q$$

is obtained from

$$\mathbb{L}_h\{T\}=\mathbb{L}_h\{S\},$$

where $\mathbb{L}$ is the differential operator representing the energy equation, Q is the concentrated heat source, $\mathbb{L}_h$ is the discrete version of $\mathbb{L}$ and S is the analytical solution to the problem

$$\mathbb{L}_h\{S\}=Q$$

in the neighbourhood of the heat source.

Equation (17) is written in a numerically non-conservative form. Its use to treat heat sources generates increasing errors as the calculation proceeds. In Reference 16 it is shown that these errors are due to the grid non-uniformity, so a fully numerically conservative scheme is used for distributed sources. Energy equation (4) is integrated in a computational cell using the divergence theorem and the co-ordinate transformation (7). The resulting equation is written as

$$(\rho c)^p\left\langle\frac{\partial T}{\partial t}\right\rangle\langle x\rangle^m\langle J\rangle=\Gamma^p\frac{\partial}{\partial U}\left[\left(\left\langle\frac{\partial T}{\partial U}\right\rangle\mathrm{AUU}+\left\langle\frac{\partial T}{\partial V}\right\rangle\mathrm{AUV}\right)\langle J\rangle x^m\right]$$
$$+\Gamma^p\frac{\partial}{\partial V}\left[\left(\left\langle\frac{\partial T}{\partial U}\right\rangle\mathrm{AVU}+\left\langle\frac{\partial T}{\partial V}\right\rangle\mathrm{AVV}\right)\langle J\rangle x^m\right]+\langle Q\rangle\langle x^m\rangle\langle J\rangle. \tag{19}$$

In equation (19) the terms in angle brackets represent an appropriate average at each cell face. The discrete version of equation (19) is obtained using centred finite differences and appropriate averages at the faces. It is

$$\mathbb{H}_0T_{i,j}^{n+1}+\mathbb{H}_1T_{i-1,j}+\mathbb{H}_2T_{i+1,j}+\mathbb{H}_3T_{i,j-1}-\mathbb{H}_4T_{i,j+1}+\mathbb{H}_5T_{i-1,j-1}+\mathbb{H}_6T_{i+1,j+1}$$
$$+\mathbb{H}_7T_{i-1,j+1}+\mathbb{H}_8T_{i+1,j-1}=\mathbb{H}_9T_{i,j}^n+\mathbb{H}_{10}, \tag{20}$$

where

$$\mathbb{H}_0=[(\rho c)^p/\delta t]x_c^mJ_c+\Gamma^p(\langle\mathrm{AUU}Jx^m\rangle_e+\langle\mathrm{AUU}Jx^m\rangle_w+\langle\mathrm{AVV}Jx^m\rangle_n+\langle\mathrm{AVV}Jx^m\rangle_s),$$
$$\mathbb{H}_1=\Gamma^p[-\langle\mathrm{AUU}Jx^m\rangle_w+\langle\mathrm{AVU}Jx^m\rangle_n/4+\langle\mathrm{AVU}Jx^m\rangle_s/4],$$
$$\mathbb{H}_2=\Gamma^p[-\langle\mathrm{AUU}Jx^m\rangle_e-\langle\mathrm{AVU}Jx^m\rangle_n/4-\langle\mathrm{AVU}Jx^m\rangle_s/4],$$
$$\mathbb{H}_3=\Gamma^p[-\langle\mathrm{AVV}Jx^m\rangle_s+\langle\mathrm{AVU}Jx^m\rangle_e/4+\langle\mathrm{AVU}Jx^m\rangle_w/4],$$
$$\mathbb{H}_4=\Gamma^p[-\langle\mathrm{AVV}Jx^m\rangle_n-\langle\mathrm{AVU}Jx^m\rangle_e/4-\langle\mathrm{AVU}Jx^m\rangle_w/4],$$
$$\mathbb{H}_5=\Gamma^p[\langle\mathrm{AUV}Jx^m\rangle_w/4+\langle\mathrm{AVU}Jx^m\rangle_s/4],$$
$$\mathbb{H}_6=\Gamma^p[-\langle\mathrm{AUV}Jx^m\rangle_e/4-\langle\mathrm{AVU}Jx^m\rangle_n/4],$$
$$\mathbb{H}_7=\Gamma^p[\langle\mathrm{AUV}Jx^m\rangle_e/4-\langle\mathrm{AVU}Jx^m\rangle_s/4],$$

$$\mathbb{H}_8 = \Gamma^{\mathrm{p}}[-\langle \mathrm{AUV}\, Jx^m\rangle_{\mathrm{e}}/4 + \langle \mathrm{AVU}\, Jx^m\rangle_{\mathrm{n}}/4],$$

$$\mathbb{H}_9 = [(\rho c)^{\mathrm{p}}/\delta t]\, x_{\mathrm{c}}^m J_{\mathrm{c}},$$

$$\mathbb{H}_{10} = Q x_{\mathrm{c}}^m J_{\mathrm{c}}.$$

Radionuclide transport problem (passive scalar transport)

The radionuclide transport equation (5) is written in terms of computational co-ordinates, via equations (7), as follows:

$$\left\langle \phi R^{\mathrm{p}} \frac{\partial C}{\partial t} \right\rangle (V - V_{\mathrm{f}}) + \left\langle R^{\mathrm{f}} \frac{\partial C}{\partial t} \right\rangle V_{\mathrm{f}} + Vu\left(\mathrm{BUX}\frac{\partial C}{\partial U} + \mathrm{BVX}\frac{\partial C}{\partial V}\right) + Vv\left(\mathrm{BUY}\frac{\partial C}{\partial U} + \mathrm{BVY}\frac{\partial C}{\partial V}\right)$$
$$+ C_{\mathrm{e}} u_{\mathrm{fe}} b_{\mathrm{e}} \cos\alpha_{\mathrm{e}} + C_{\mathrm{f}} v_{\mathrm{fn}} b_{\mathrm{n}} \cos\alpha_{\mathrm{n}} - C_{\mathrm{w}} u_{\mathrm{fw}} b_{\mathrm{w}} \cos\alpha_{\mathrm{w}} - C_{\mathrm{s}} v_{\mathrm{fs}} b_{\mathrm{s}} \cos\alpha_{\mathrm{s}}$$
$$= V\phi D^{\mathrm{p}}\left(\mathrm{BUU}\frac{\partial^2 C}{\partial U^2} + \mathrm{BVV}\frac{\partial^2 C}{\partial V^2} + \mathrm{BUV}\frac{\partial^2 C}{\partial U \partial V} + (\mathrm{BU} + m\,\mathrm{BUX}\, x^{-m})\frac{\partial C}{\partial U}\right.$$
$$\left. + (\mathrm{BV} + m\,\mathrm{BVX}\, x^{-m})\frac{\partial C}{\partial V}\right) + R_{\mathrm{f}}\left(\mathrm{EUU_e}\frac{\partial C}{\partial U} b_{\mathrm{e}} \cos\alpha_{\mathrm{e}} + \mathrm{FVV_n}\frac{\partial C}{\partial V} b_{\mathrm{n}} \cos\alpha_{\mathrm{n}}\right.$$
$$\left. - \mathrm{EUU_w}\frac{\partial C}{\partial U} b_{\mathrm{w}} \cos\alpha_{\mathrm{w}} - \mathrm{FVV_s}\frac{\partial C}{\partial V} b_{\mathrm{s}} \cos\alpha_{\mathrm{s}}\right) - \lambda[\phi R^{\mathrm{p}}(V - V_{\mathrm{f}}) + R^{\mathrm{f}} V_{\mathrm{f}}]. \tag{21}$$

The discrete version of equation (21) is obtained using centred differences; then

$$\mathbb{M}_0 C_{i,j}^{n+1} + \mathbb{M}_1 C_{i-1,j} + \mathbb{M}_2 C_{i+1,j} + \mathbb{M}_3 C_{i,j-1} + \mathbb{M}_4 C_{i,j+1} + \mathbb{M}_5 C_{i-1,j-1} + \mathbb{M}_5 C_{i+1,j+1}$$
$$+ \mathbb{M}_6 C_{i-1,j+1} + \mathbb{M}_6 C_{i+1,j-1} = \mathbb{M}_7 C_{i,j}^n, \tag{22}$$

where

$$\mathbb{M}_0 = [\phi R_{\mathrm{p}}(V - V_{\mathrm{f}}) + R_{\mathrm{f}} V_{\mathrm{f}}](1/\delta t + \lambda) + u_{\mathrm{fi}+1,j} b_{\mathrm{e}} \cos\alpha_{\mathrm{e}} \mathrm{DU}_{i+1,j} - u_{\mathrm{fi},j} b_{\mathrm{o}} \cos\alpha_{\mathrm{o}}(1 - \mathrm{DU}_{i,j})$$
$$+ u_{\mathrm{fi},j+1} b_{\mathrm{n}} \cos\alpha_{\mathrm{n}} \mathrm{DV}_{i,j+1} - v_{\mathrm{fi},j} b_{\mathrm{s}} \cos\alpha_{\mathrm{s}}(1 - \mathrm{DV}_{i,j}) + 2D^{\mathrm{p}}\phi V(\mathrm{AUU}_{i,j} + \mathrm{AVV}_{i,j})$$
$$+ D^{\mathrm{f}}(\mathrm{EUU}_{i,j} b_{\mathrm{w}} \cos\alpha_{\mathrm{w}} + \mathrm{EUU}_{i+1,j} b_{\mathrm{e}} \cos\alpha_{\mathrm{e}} + \mathrm{FVV}_{i,j} b_{\mathrm{s}} \cos\alpha_{\mathrm{s}} + \mathrm{FVV}_{i,j+1} b_{\mathrm{n}} \cos\alpha_{\mathrm{n}}),$$

$$\mathbb{M}_1 = (-u_{i+1/2,j+1/2}\mathrm{AUX}_{i,j} - v_{i+1/2,j+1/2}\mathrm{AUY}_{i,j})/2 - u_{\mathrm{fi},j} b_{\mathrm{w}} \cos\alpha_{\mathrm{w}} \mathrm{DU}_{i,j}$$
$$+ D^{\mathrm{p}}\phi V[-\mathrm{AUU}_{i,j} + (\mathrm{AU}_{i,j} + x^{-m}\mathrm{AUX}_{i,j})/2] - D^{\mathrm{f}} \mathrm{EUU}_{i,j} b_{\mathrm{w}} \cos\alpha_{\mathrm{w}},$$

$$\mathbb{M}_2 = (+u_{i+1/2,j+1/2}\mathrm{AUX}_{i,j} + v_{i+1/2,j+1/2}\mathrm{AUY}_{i,j})/2 + u_{\mathrm{fi},j} b_{\mathrm{e}} \cos\alpha_{\mathrm{e}}(1 - \mathrm{DU}_{i+1,j})$$
$$+ D^{\mathrm{p}}\phi V[-\mathrm{AUU}_{i,j} + (-\mathrm{AU}_{i,j} - x^{-m}\mathrm{AUX}_{i,j})/2] - D^{\mathrm{f}}\mathrm{EUU}_{i+1,j} b_{\mathrm{e}} \cos\alpha_{\mathrm{e}},$$

$$\mathbb{M}_3 = (-u_{i+1/2,j+1/2}\mathrm{AVX}_{i,j} - v_{i+1/2,j+1/2}\mathrm{AVY}_{i,j})/2 - v_{\mathrm{fi},j} b_{\mathrm{s}} \cos\alpha_{\mathrm{s}} \mathrm{DV}_{i,j}$$
$$+ D^{\mathrm{p}}\phi V[-\mathrm{AVV}_{i,j} + (\mathrm{AV}_{i,j})/2] - D^{\mathrm{f}}\mathrm{FVV}_{i,j} b_{\mathrm{s}} \cos\alpha_{\mathrm{s}},$$

$$\mathbb{M}_4 = (u_{i+1/2,j+1/2}\mathrm{AVX}_{i,j} + v_{i+1/2,j+1/2}\mathrm{AVY}_{i,j})/2 + v_{\mathrm{fi},j+1} b_{\mathrm{n}} \cos\alpha_{\mathrm{n}}(1 - \mathrm{DV}_{i,j+1})$$
$$+ D^{\mathrm{p}}\phi V[-\mathrm{AVV}_{i,j} + (-\mathrm{AV}_{i,j})/2] - D^{\mathrm{f}}\mathrm{FVV}_{i,j+1} b_{\mathrm{n}} \cos\alpha_{\mathrm{n}},$$

$$\mathbb{M}_5 = -D^{\mathrm{p}}\phi V \mathrm{AUV}_{i,j}/4,$$

$$\mathbb{M}_6 = -\mathbb{M}_5,$$

$$\mathbb{M}_7 = [\phi R_{\mathrm{p}}(V - V_{\mathrm{f}}) + R_{\mathrm{f}} V_{\mathrm{f}}]/\delta t.$$

After the thermal and hydrodynamic problems are advanced in time, equation (22) is solved using an implicit scheme. The boundary conditions, namely specified concentrations or specified mass fluxes, are explicitly incorporated.

RESULTS

The algorithms described above have been applied to the prediction of many cases of interest to us,[13] giving support to the accuracy of the analysis. The most significant examples are summarized in this section.

The first case[4] is a calibration example of the 3D code consisting of the flow driven by an imposed geothermal gradient towards a disc-shaped horizontal fracture. The fracture is connected to the surface by a vertical rectangular fracture. This situation is sketched in Figure 2 and was first studied by Wang *et al.*[17] However, those authors considered that the central part of the disc-shaped fracture represented a disc repository with a given heat power, and considered a 1D approximate analysis which is simulated with the grid shown in the figure. It consists of 31×30 nodes in the horizontal plane and five nodes along the vertical direction. The difference in node number on the horizontal plane is due to the variable centring and the form in which the vertical fracture is represented. The dimensions of the scenario are also shown in Figure 2. The permeability of the fracture is $k_f = 10^{-9}$ m^2 and the aperture of the fracture is $b = 10^{-3}$ m. Since the model considers a porous–fractured rock, this situation can be modelled if the corresponding permeability of the rock matrix is set very much lower than that for the fractures ($k_p = 10^{-30}$ m^2 is used). The boundary conditions were set as follows:

(i) homogeneous medium—zero velocity on all boundaries
(ii) fracture system—constant pressure at the top boundary and free-slip boundaries at the disc perimeter.

The fluid velocity in the vertical fracture, imposing a uniform temperature gradient, compares within 8% with the results from the 1D analysis of Wang *et al.* for the same conditions.

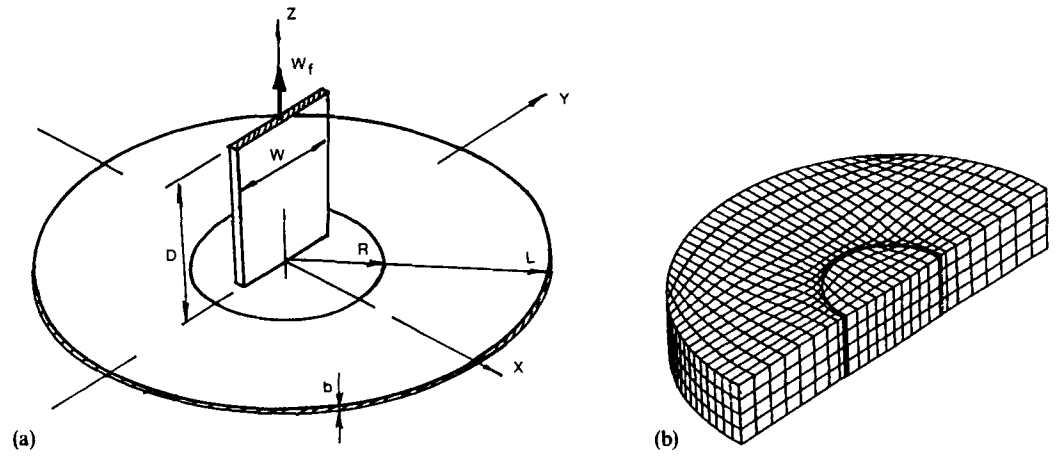

Figure 2. Natural convection flow from a horizontal disc-shaped fracture towards a vertical one: (a) problem definition and constants ($W = 780$ m, $D = 987$ m, $L = 5000$ m, $R = 1500$ m, $k_f = 10^{-9}$ m^2); (b) partial view of the 3D grid ($31 \times 30 \times 5$ nodes)

The second set[4] of calculations consists of the prediction of three benchmark problems of the HYDROCOIN project,[18] of interest in the case of crystalline rocks. The first is the prediction of the transient flow from a borehole in a consolidating porous medium (case 1, level 1). Figure 3 shows a sketch of the problem and its boundary conditions, namely:

(i) impermeable walls at the top and bottom boundaries
(ii) specified pressure ($P=0$) at the right boundary
(iii) specified pressure at the left boundary according to the law

$$P(t)=1-e^{-(t/0\cdot1)} \quad (t \text{ in seconds}).$$

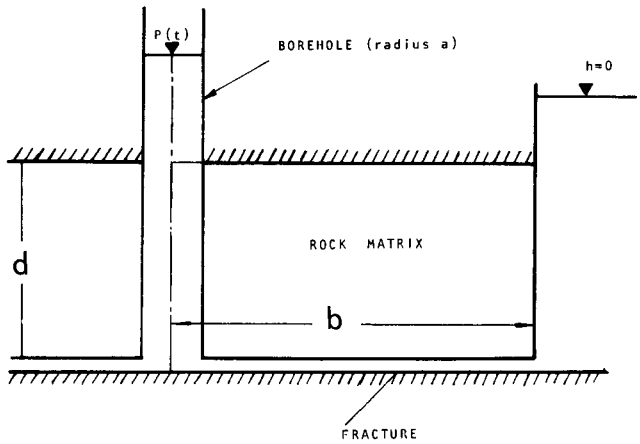

Figure 3. Flow from a borehole in a consolidating porous soil with a fracture in the bottom boundary HYDROCOIN case 1, level 1 (adapted from Reference 18)

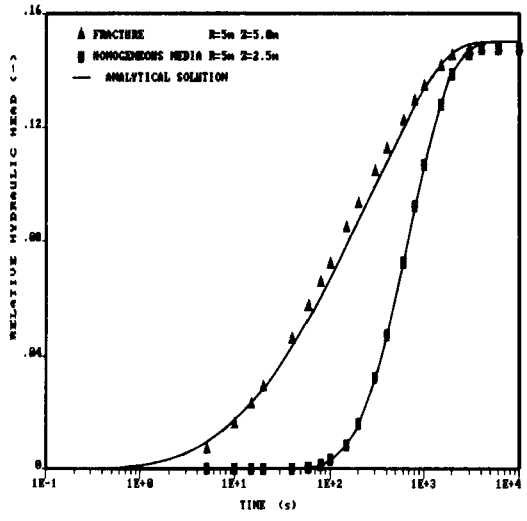

Figure 4. Flow from a borehole in consolidating porous soil. Solution for the time-dependent hydraulic head. HYDROCOIN problem 1, level 1. Maximum error 2% at $R=5$ m

The hydraulic conductivities are $K_p = 10^{-7}\ m\,s^{-1}$ and $K_f = 10^{-6}\ m\,s^{-1}$ for the homogeneous rock and the fracture respectively. The corresponding specific storativities are $S^p = 10^{-7}\ m^{-1}$ and $S^f = 10^{-8}\ m^{-1}$ respectively. Figure 4 shows the results using a grid of 22×24 nodes compared with the analytical solution.[18] The maximum error does not exceed 2%.

The second case consists of the predictions of the steady flow in a rock mass intersected by two permeable fractured zones (case 2, level 1).[18] Figure 5 shows the physical domain and the grid considered (35×28 nodes). The hydraulic conductivities were $K_p = 10^{-8}\ m\,s^{-1}$ and $K_f = 10^{-6}\ m\,s^{-1}$ for the rock and the fractured zones respectively; the widths of the fractured zones were $b = 15$ m (A–A) and $b = 10$ m (B–B). For the top boundary (ground surface) the boundary conditions were $P = gz$. Water-impervious vertical and bottom boundaries were assumed. The pressure profiles at different depths ($z = 0, -200, -400, -600, -800$) are compared with the proposed benchmark solution.[18] Figure 6 shows the pressure distribution at $z = -400$ m. The error does not exceed 2·5% in all cases. Errors decreased smoothly with increasing discretization. Figure 7 shows a vector plot of the steady state flow field.

The next case consists of the prediction of the thermal convection in a saturated porous medium driven by a spherical heat source (case 4, level 1).[18] The medium is homogeneous and isotropic. The heat source is spatially uniform and decays with time according to an exponential law. The parameters are

sphere radius	250 m
initial power	10 MW
decay constant	$7{\cdot}3215 \times 10^{10}\ s^{-1}$
permeability	$10^{-16}\ m^2$
rock density	$2600\ kg\,m^{-3}$
heat capacity	$879\ J\,kg^{-1}\,K^{-1}$.

A 2D code using axisymmetric grids is employed. The upper half of the grid is shown in Figure 8. The analytical solution is imposed at all boundaries, except at the symmetry edge. Figure 9 shows the time-dependent temperature along the vertical centreline. The maximum errors in temperature and pressure do not exceed 5% (see Figure 10).

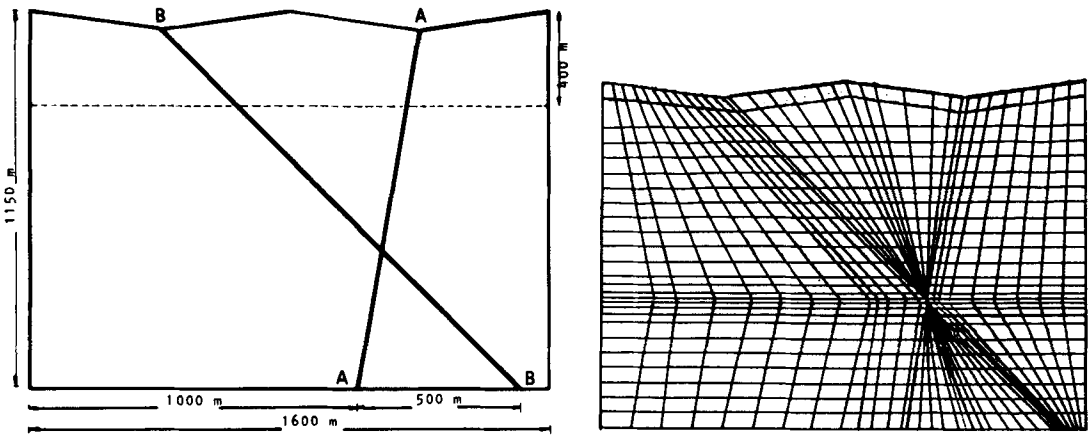

Figure 5. Steady state flow in a rock mass intersected by two fractured zones. HYDROCOIN problem 2, level 1. (a) Problem definition (adapted from Reference 18); (b) 2D grid of 35×28 nodes

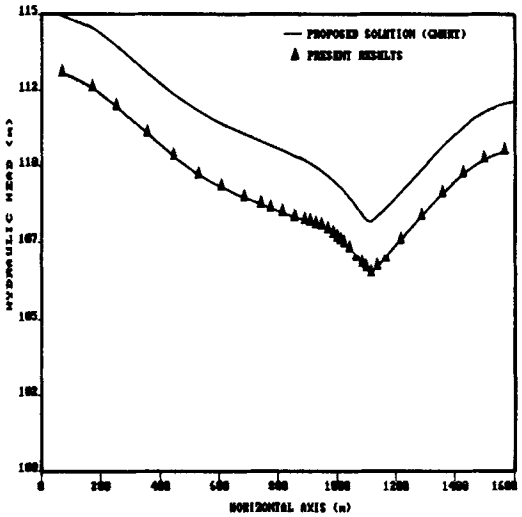

Figure 6. Steady state flow in a rock mass intersected by two fractured zones. HYDROCOIN problem 2, level 1. Hydraulic head distribution at $z = -400$ m. Maximum error 2·5%

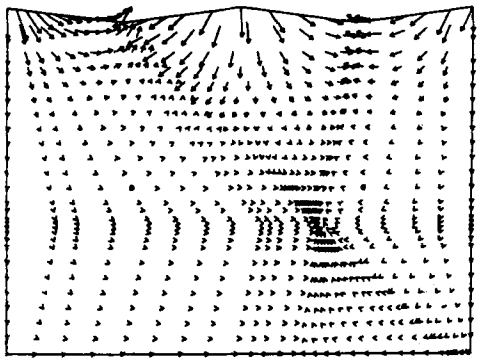

Figure 7. Steady state flow in a rock mass intersected by two fractured zones. HYDROCOIN problem 2, level 1. Fluid flow vector plot

The next example refers to flow past an isolated fracture and was taken from Reference 9. It consists of the prediction of the flow in a homogeneous porous medium with an isolated fracture parallel to the velocity field at an infinite distance. Figure 11(a) shows the physical domain. This case is appropriate to illustrate a typical configuration of 1D paths in an otherwise continuous medium. Figure 11(b) shows a partial view of the grid used to solve the problem. The results are obtained with a grid of 25×14 nodes. Boundary conditions are imposed at infinity as given by the analytical solution in Reference 19. It is interesting to point out that the grid is very coarse so the solution is obtained after applying the technique of singularity extraction mentioned before. The permeabilities are $k = 10^{-15}$ m^2 and $k_f = 10^{-7}$ m^2 for the homogeneous rock and the fracture respectively. The maximum aperture of the fracture is 0·01 m. Figure 12(a) shows a vector plot of

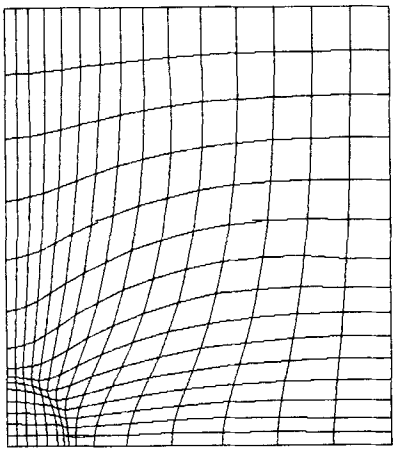

Figure 8. Transient thermal convection in a saturated porous medium. HYDROCOIN problem 4, level 1. Upper half of the grid (16 × 31 nodes)

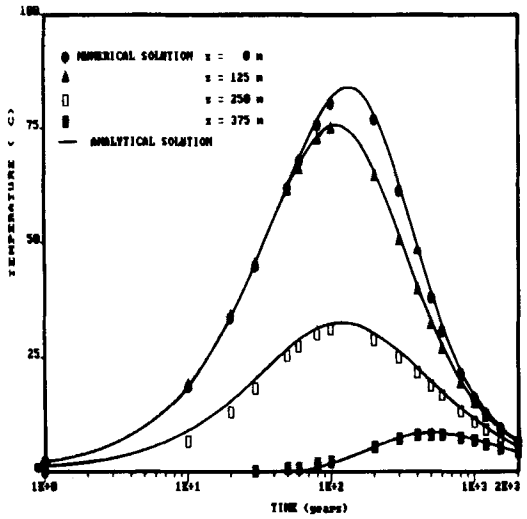

Figure 9. Transient thermal convection in a saturated porous medium. HYDROCOIN problem 4, level 1. Time-dependent temperature rise along the vertical centreline

the resulting flow field. The results obtained compare reasonably well with the analytical ones (see Figure 12(b)). Errors are of the order of 9% in the immediate vicinity of the fracture and tend to zero towards the limits of the domain.

The next case[4] considers the results of Tang *et al.*,[20] who studied the influence of a porous matrix on the diffusion of a radioactive tracer. The boundary conditions (see Figure 13) are such that flow and advection occur along the discrete fracture. Only molecular diffusion is allowed in the rock matrix. The geometry and dimensions are shown in Figure 13. The grid employed has

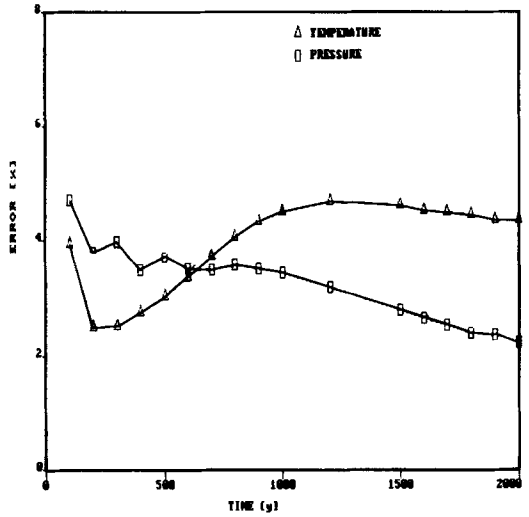

Figure 10. Transient thermal convection in a saturated porous medium. HYDROCOIN problem 4, level 1. Time evolution of the maximum errors: temperature, 5·0%; pressure 2·5%

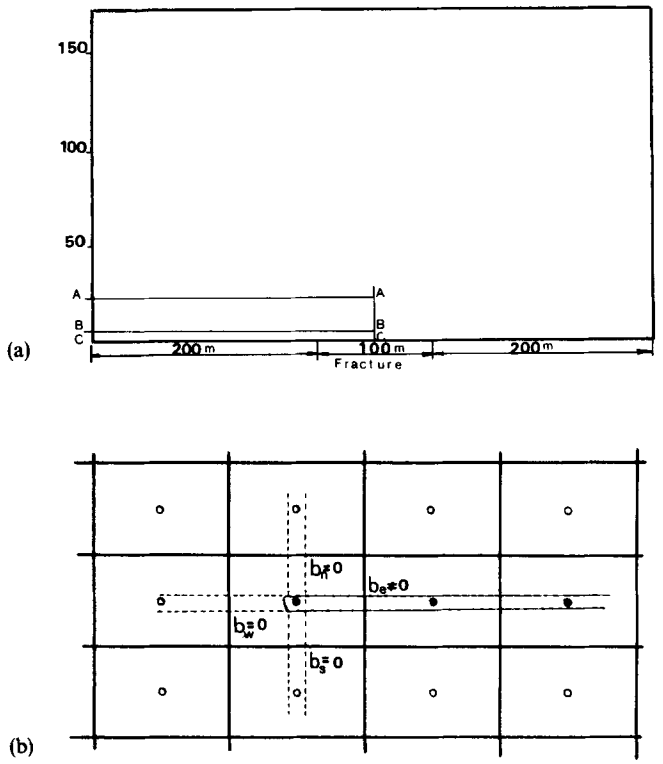

Figure 11. Steady state fluid flow in a porous medium with a single fracture embedded in the centre of the domain: (a) problem definition; (b) grid set-up

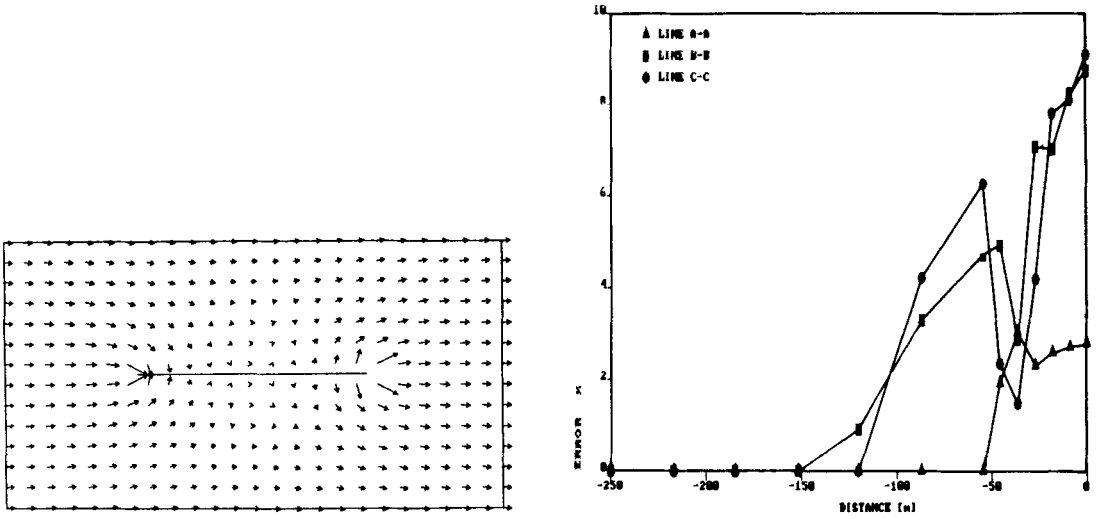

(a) (b)

Figure 12. Steady state fluid flow in a porous medium with a single fracture embedded in the centre of the domain: (a) steady state velocity vector plot; (b) errors in the computed solution

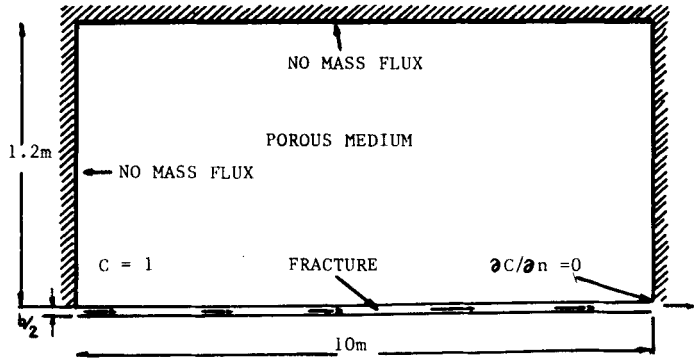

Figure 13. Solute transport in a fractured–porous medium. Physical domain and boundary conditions (adapted from Reference 9)

25×21 nodes. It is refined in the vicinity of the fracture and is almost uniform in the horizontal direction. The physical parameters are set to:

$D_f = 5{\cdot}95 \times 10^{-8}\ \mathrm{m^2\,s^{-1}}$
$D_p = 1{\cdot}60 \times 10^{-10}\ \mathrm{m^2\,s^{-1}}$
$u_f = 1{\cdot}17 \times 10^{-7}\ \mathrm{m\,s^{-1}}$
$b = 10^{-4}\ \mathrm{m}$
$\phi = 0{\cdot}01$
$\lambda = 12{\cdot}35\ \mathrm{yr}$
$R = 1.$

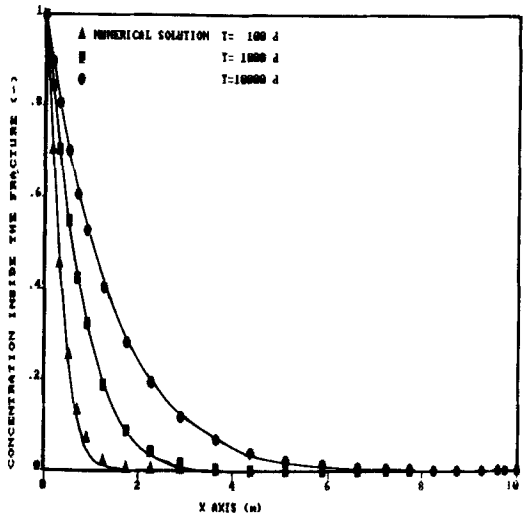

Figure 14. Finite difference solution for the solute transport in a fractured–porous medium with concentration profiles along the fracture. Maximum error 2%

Figure 14 shows a comparison of the results obtained for this restricted problem with the analytical solution.[20] This graphic comparison indicates very good agreement between results.

In the following examples, two hypothetical configurations of a high-level radioactive waste repository emplacement are considered. The repository is located at a depth of 500 m. Its dimensions are 500 m by 500 m in the horizontal directions and about 10 m in the vertical direction. It can be modelled as a plane heat source.[1] Only the heat diffusion is considered in the porous medium. This approximation makes it possible to uncouple the hydrodynamic problem from the thermal one. The heat produced by the decay of the fission products varies according to the law[1]

$$Q = Q_0(Ae^{-\alpha t} + Be^{-\beta t}),$$

where

$Q_0 = 5{\cdot}25\ \mathrm{W\,m^{-2}}$
$A = 0{\cdot}901$
$\alpha = 2{\cdot}373 \times 10^{-2}\ \mathrm{yr^{-1}}$
$B = 0{\cdot}099$
$\beta = 1{\cdot}610 \times 10^{-3}\ \mathrm{yr^{-1}}$.

The fluid flow boundary conditions are set as follows:

(i) bottom boundary—impermeable, because the hydraulic conductivity at a depth greater than or equal to 1500 m is low enough to consider that no flux occurs
(ii) left and right boundaries—impervious, because they are taken to be located below the valley or at the top of mountains, which nearly prevents the flow of water to the surrounding regions
(iii) top boundary—the water table is taken to be coincident with the topography; this approximation is suitable for crystalline rocks and in this case the pressure can be imposed at the boundary.

The first case considers a repository located below a hill in the vicinity of a zone with two permeable fractured zones. The flow is induced not only by the thermal gradients but also by the topography. The dimensions of the integration domain are the same as in the third verification case (HYDROCOIN project level 1, case 2), except that the slopes of the hills are reduced from 0·125 to 0·0125 m m^{-1}. In this way the hydraulic and thermal gradients have the same magnitude. A grid of 35 × 28 nodes similar to the one shown in Figure 5(b) is used in the calculations. Figure 15(a) shows a vector plot of the velocity field before the repository is installed. In this case the flow is oriented towards the fractures, especially towards the one denoted by A–A. This fracture also acts as the collector of the fluid captured by the other fracture. Figure 15(b) shows a vector plot of the velocity field 1000 yr after the repository was installed. The flow pattern is not very much altered in the first 300 m, because the hydraulic gradients govern the flow. At a depth of 500 m the

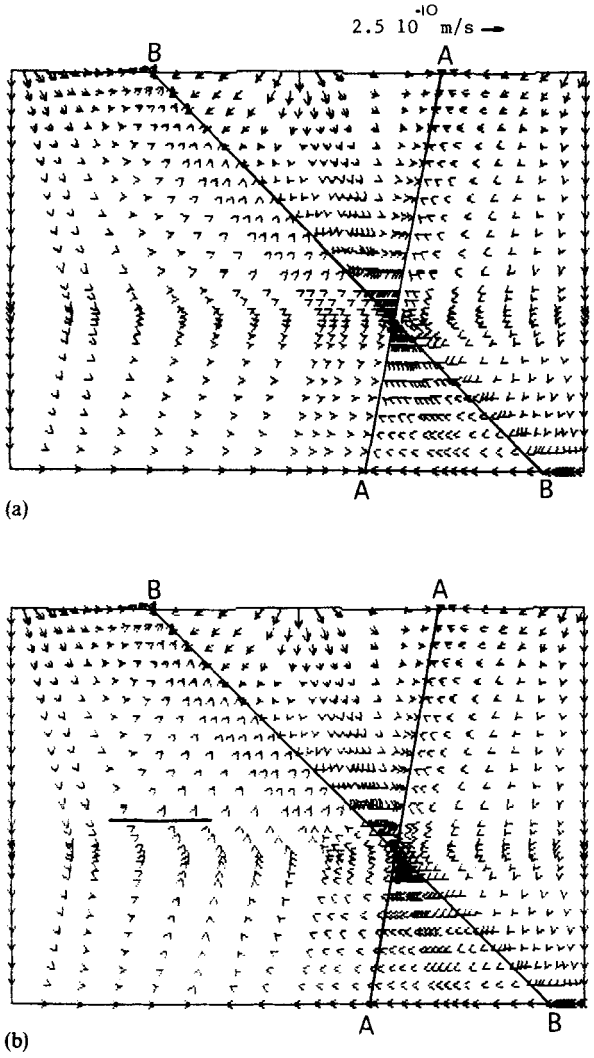

Figure 15. Repository located below a hill in the vicinity of two permeable fracture zones: (a) velocity vector plot before the repository is installed; (b) velocity vector plot 1000 yr after the repository is installed.

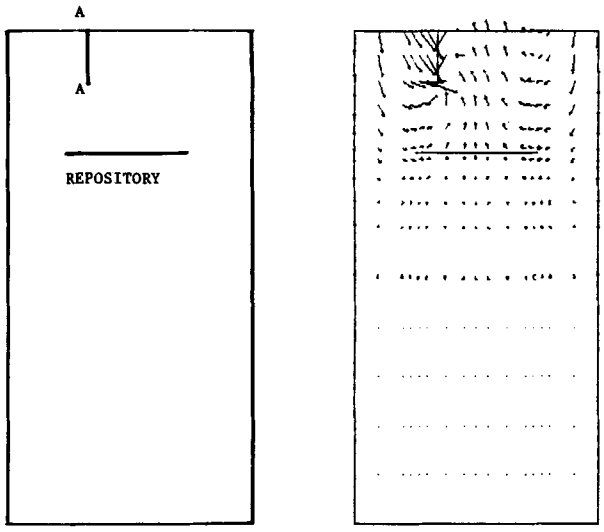

Figure 16. Repository located below a horizontal surface in the vicinity of a fracture: (a) integration domain; (b) velocity vector plot at $t = 1000$ yr

thermal gradients impose a dramatic change on the flow pattern. The fluid is collected by fracture B–B. Moreover, the flow in fracture A–A is reversed and diverted to the collector fracture (B–B). The flow at depths greater than 600 m is forced mainly by the thermal gradients and the configuration of the fractures is not very important.

The scenario of the second application problem is shown in Figure 16(a). The repository is located 500 m below a horizontal surface. The domain of integration is 2000 m along y per 1000 m along x. A vertical fracture, denoted by A–A, is located 200 m from the centre of the repository. The aperture of the fracture is 10 m and its length is 200 m. The hydraulic conductivity of the rock at 500 m depth is $K_p = 10^{-9}$ m s^{-1} and the hydraulic conductivity of the fracture is $K_f = 10^{-5}$ m s^{-1}. The hydraulic conductivity of the rock varies according to the law[21]

$$K_p(y) = K_p(500)e^{0.0092(500-y)}.$$

As may be seen in Figure 16(b), the flow field is strongly influenced by the fracture. In its absence the thermal gradients tend to generate recirculation cells. These cells disappeared completely owing to the presence of the fracture. Moreover, the fluid is collected from the right side of the top boundary, diverted to the repository and then collected by the fracture. Below 900 m almost no flow exists because the permeability is too low.

CONCLUSIONS

A numerical method for the prediction of the hydrodynamics of fractured–porous media has been developed. The use of boundary-fitted grids allows the fitting of discrete fractures in the bulk of the porous matrix. These fractures usually define the flow pattern. The method covers 2D unsteady flow in natural circulation driven by thermal sources, consolidating media and three dimensions in steady problems. The discrete fractures are included in the control volumes as one-dimensional paths of variable aperture in 2D (curved surfaces in 3D). In this way the working

scenario may approximate conditions of interest in the modelling of flows in geological applications. The techniques have been verified against previous results and benchmark examples. As a general comment on the accuracy of the results, it may be pointed out that the criterion was to obtain agreement between present and previous results to within a few per cent. The goal here was to show that this could be accomplished with a relatively coarse discretization. The effect of grid distortions has been considered previously[16, 22] and is mainly responsible for the errors reported. However, in the case of regular grids, errors can be attributed to coarse discretization in zones of steep variation of the dependent variables. The results obtained agree with those proposed within a few per cent. The salient features of the method, namely fitting the discrete fractures and their inclusion in the control volumes, made it possible to develop an accurate prediction technique. Experimental results in our main field of interest are scarce but are beginning to emerge. The validation of the codes will be the subject of future work.

ACKNOWLEDGEMENTS

The authors thank the reviewers for their many valuable suggestions and Hilde Torres Perrin for reading the manuscript.

REFERENCES

1. J. C. Ferreri and M. Ventura, 'Numerical aspects of the study of regional thermal impact of radioactive waste repository', *Nucl. Eng. Design*, **86**, 253–263 (1985).
2. J. C. Ferreri and G. M. Grandi, 'Models for the study of local effects produced by a high-level radioactive waste repository', in C. Taylor, M. D. Olson, P. M. Gresho and W. G. Habashi (eds), *Numerical Methods in Laminar and Turbulent Flows*, Vol. 2, Pineridge Press, Swansea, 1985, pp. 1257–1267.
3. G. M. Grandi and J. C. Ferreri, 'FRACTURE-BFC: a computer code for the numerical prediction of hydrodynamics in fractured–porous media', in S. Idelsohn (ed.), *Proc. MECOM'85, 15–18 October 1985, Mecánica Computacional*, Vol. 3, AMCA, Santa Fe, Argentina, pp. 301–323 (1986).
4. G. M. Grandi and J. C. Ferreri, 'Boundary-fitted finite-difference calculation of fluid flow and scalar transport in fractured–porous media', in H. Niki and M. Kawahara (eds), *Proc. Int. Conf. on Computational Methods in Flow Analysis*, Vol. 1, Okayama University of Science, Okayama, Japan, 5–8 September 1988, pp. 611–618.
5. R. R. Peters and E. A. Klavetter, 'A continuum model for water movement in an unsaturated fractured rock mass', *Water Resources Res.*, **24**, 416–430 (1988).
6. T. Narasimhan, 'Multidimensional numerical simulation of fluid flow in fractured porous media', *Water Resources Res.*, **18**, 1235–1247 (1982).
7. J. C. Long, 'Approaches to fracture modelling for field studies', *Proc. GEOVAL 1987*, Stockholm, 7–9 April 1987, Swedish Nuclear Power Inspectorate, Sweden (1988).
8. K. Pruess and T. Narasimhan, 'A practical method for modelling fluid and heat flow in fractured–porous media', *J. Soc. Petrol. Eng.*, 14–26 (February 1985).
9. R. Baca, R. Arnett and D. W. Langford, 'Modelling fluid flow in fractured–porous rock masses by finite element techniques', *Int. j. numer. methods fluids*, **4**, 337–348 (1984).
10. D. P. Hodgkinson, 'A mathematical model for hydrothermal convection around a radioactive waste depository in hard rock', *Ann. Nucl. Energy*, **7**, 313–334 (1980).
11. B. Martinez and J. C. Ferreri, 'SOLA-BFC: a computer code for unsteady fluid flow calculation with boundary-fitted co-ordinates', in A. Ferrante (ed.), *Anales III Congr. Latinoamericano Sobre Metodos Computacionales en Ingenieria*, Asociación Lat. Met. Compt. en Ingeniería, Buenos Aires, 1982, pp. 614–630.
12. M. J. Hoofer (compiler), 'AERE Harwell subroutine library—a catalogue of subroutines', *AERE-R9185*, 1980.
13. G. M. Grandi, 'Métodos computaciona les de la hidrodinámica de medios porosos fracturados', *Ph.D. Thesis*, Instituto Balseiro, Universidad Nacional de Cuyo, Argentina, 1988.
14. J. C. Ferreri, 'A note on the steady-state advection–diffusion equation', *Int. j. numer. methods fluids*, **5**, 593–596 (1985).
15. J. C. Ferreri, 'A new alternative for decision-making concerning the cost/accuracy controversy', in S. Idelsohn (ed.), *Proc. MECOM'85, 15–18 October 1985, Mecánica Computacional*, Vol. 3, AMCA, Santa Fe, Argentina, pp. 129–139 (1986).
16. G. M. Grandi and J. C. Ferreri, 'On the solution of heat conduction problems involving heat sources via boundary fitted grids', *Commun. Appl. Numer. Methods*, **5**, 1–6 (1989).
17. J. Wang, C. Tsang and N. Cook, 'A study of regional temperature and thermohydrologic effects of an underground repository for nuclear wastes in hard rock', *J. Geophys. Res.*, **86**, 3759–3770 (1981).

18. 'HYDROCOIN: final definitions of the test problems included in level 1 of the HYDROCOIN project', Kemakta Consultants AB, Stockholm, Sweden, 1986.
19. O. Strack, 'Analytic modelling of flow in permeable fissured medium', *PNL 4005*, Pacific Northwest Laboratory, Richland, WA, 1981.
20. D. H. Tang, E. O. Frind and E. A. Sudicky, 'Contaminant transport in fractured porous media: analytical solution for a single fracture', *Water Resources Res.*, **17**, 555–564 (1981).
21. R. Thunvik and C. Braester, 'Hydrothermal conditions around a radioactive waste repository', *KBS TEKNISK Rapport 80-19*, Sweden, 1980.
22. J. C. Ferreri, and M. A. Ventura, 'On the accuracy of boundary-fitted finite-difference calculations', *Int. j. numer. methods in fluids*, **4**, 359–375 (1984).